





SUstainable solutions for affordable REtroFIT of domestic buildings

Call: H2020-LC-SC3-2018-2019-2020

Topic: LC-SC3-EE-1-2018-2019-2020

Type of action: IA

Grant Agreement number	894511
Project acronym	SUREFIT
Project full title	SU stainable solutions for affordable RE tro FIT of domestic buildings
Due date of deliverable	30/11/2021
Lead beneficiary	University of Nottingham (UNOTT)
Other authors	Instituto de Soldadura e Qualidade (ISQ)

WP4 - Deliverable D 4.6
Heat recovery unit



Dissemination Level

PU	Public	х
со	Confidential, only for members of the consortium (including the Commission Services)	
Cl	Classified, as referred to in Commission Decision 2001/844/EC	

Document History

Version	Date	Authors	Description	
1	30/11/2021	University of Nottingham	First draft of D4.6	
2	12/01/2022	ISQ	Reviewed draft	
3	27/04/2022	University of Nottingham	Reviewed draft	
4	04/05/2022	University of Nottingham	Draft for reviewers	
5	13/05/2022	University of Nottingham	Final version for Coordinator	

Disclaimer

This document is the property of the **SUREFIT** Consortium.

This document may not be copied, reproduced, or modified in the whole or in the part for any purpose without written permission from the **SUREFIT** Coordinator with acceptance of the Project Consortium.

This publication was completed with the support of the European Commission under the *Horizon 2020 research and innovation programme*. The contents of this publication do not necessarily reflect the Commission's own position. The documents reflect only the author's views and the Community is not liable for any use that may be made of the information contained therein.

This project has received funding from the European Union's Horizon 2020 research and innovation programme under grant agreement No **894511**.



Contents

T	able of	figures	4
T	able of	tables	5
A	bbrevia	rtions	6
Ρι	ublisha	ble summary	7
In	troduc	tion	8
1	Sur	nmary	9
2	Con	cept and modelling	10
	2.1 Sys	tem configurations	11
	2.2	Numerical modelling	
	2.2.1	•	
	2.2.2		
	2.2.3		
3	Ехр	erimental and validation	17
	3.1	Experimental	17
	3.1.1	Determination of effective thermal conductivity	17
	3.2	Validation	18
	3.2.1	. Analytical formulation	18
	3.2.2	CFD validation	19
4	Resi	ults and discussion	22
	4.1	Parametric analysis	22
	4.2	Thermal comfort	25
5	Con	clusions	28
Re	eferenc	es	29





Table of figures

Fig. 1. 3D view of window integrated system (a), heat recovery unit -integrated to window frame (b), and heat reco	VERY
PROTOTYPE (C)	9
FIG. 2. WINDOW HEAT RECOVERY SYSTEM INTEGRATED WITH BUILDING (WINTER EXAMPLE)	11
FIG. 3. THERMAL RESISTANCE NETWORK BETWEEN HEAT PIPES AND AIR IN COLD AND HOT SIDES	12
FIG. 4. THE FLOWCHART OF THE SOLUTION METHOD	14
FIG. 5. (A) COMPUTATIONAL MESH OF THE HEAT PIPES. (B) COMPUTATIONAL MESH OF THE SMALL ROOM	16
FIG. 6. WINDOW HEAT RECOVERY PROTOTYPE USED IN THE EXPERIMENTS	17
FIG. 7. EFFECTIVE THERMAL CONDUCTIVITY FOR THE TEMPERATURE DIFFERENCES	18
FIG. 8. COMPARISON BETWEEN EXPERIMENTAL AND NUMERICAL RESULTS FOR DIFFERENT TEST CONDITIONS	19
Fig. 9. CFD simulation results with an inlet temperature of 15 $^{\circ}$ C and inlet velocity of 0.93 m/s: (a) Temperature and	D (B)
VELOCITY MAGNITUDE	20
FIG. 10. TEMPERATURE PROFILE IN AIR AND HEAT PIPE ALONG THE FLOW DIRECTION OF THE WINDOW HEAT RECOVERY SYSTEM	22
FIG. 11. IMPACT OF MAXIMUM TEMPERATURE DIFFERENCE ON THE THERMAL EFFECTIVENESS WITH VENTILATION RATE VARIED BETWEE	
то 60 м³/н	
Fig. 12. Impact of heat pipe numbers on the thermal effectiveness with ventilation rate varied between $10 \text{ to } 60 \text{ m}^3/\text{s}$	н 24
FIG. 13. CFD CALCULATED RELATIVE TOTAL PRESSURE FROM INLET TO OUTLET OF THE WHR SYSTEM	
Fig. 14. System pressure drop under ventilation rates varied between $10-60 \mathrm{m}^3/\mathrm{h}$	25
FIG. 15. AIR TEMPERATURE AND VELOCITY DISTRIBUTION IN THE HORIZONTAL SECTION AT DIFFERENT DISTANCES FROM THE INLET UND	
10 m³/h ventilation rate without heat recovery	26
FIG. 16. AIR TEMPERATURE AND VELOCITY DISTRIBUTION IN THE HORIZONTAL SECTION AT DIFFERENT DISTANCES FROM THE INLET UND	
10 m³/h (a), 30 m³/h (b) and 60 m³/h (c) ventilation rates with heat recovery	27

13/05/2022





Table of tables

Table 1 Geometric parameters of the window heat recovery system	14
TABLE 2: COMPARISON BETWEEN MEASURED AND MODELLED OUTLET TEMPERATURE	19
TABLE 3 COMPARISON BETWEEN CFD SIMULATION AND NUMERICAL OUTLET TEMPERATURES	





Abbreviations

WHR Window heat recovery

FVM Finite Volume Method

CFD Computational fluid dynamics





Publishable summary

This report addresses the numerical and experimental performance analysis of a windows heat recovery system made of heat pipes. For modelling, the heat pipe is considered as a pseudo solid material with high value of effective thermal conductivity. An experimental investigation using a window heat recovery prototype was carried out to predict the value of effective thermal conductivity of the heat pipes and to validate the numerical model. After validation, a parametric analysis was conducted to investigate the performance of the recovery system for different working conditions (mass flow rate and temperature difference between exhausted and supplied air). Based on the performance obtained in the parametric analysis, energy performance in building and thermal comfort is also evaluated with the support of CFD analysis. It is found that the effectiveness of window heat recovery made of heat pipes depends on ventilation rate and temperature difference between exhausted and supplied air. Increasing ventilation rates and temperature differences decrease the effectiveness. For ventilation rate between 10 - 60 m3/h and temperature difference 10 - 30°C, effectiveness between 10 - 300°C, effectiveness

The work reported here was published as "An innovative window heat recovery (WHR) system with heat pipe technology: Analytical, CFD, experimental analysis and building retrofit performance, January 2021. SSRN Electronic Journal, http://dx.doi.org/10.2139/ssrn.3960587"



Introduction

Leading Beneficiary: University of Nottingham (UNOTT)

Participants: Instituto de Soldadura e Qualidade (ISQ)

Task description:

The work package involves fabricating and testing the key components and assembling the components into complete prototypes of technologies. The technologies will be tested in the lab to assess their performance under the nominal set conditions. The testing results will be used to modify and improve the design of the final prototypes, if necessary, which will be used in WP6 (field tests). The availability of this prototype system for field trials will be milestone 3. UNOTT is the work package leader.

Task 4.2: Produce solutions for energy efficient facilities (UNOTT, M7-M17)

• UNOTT will produce window heat recovery devices.

This deliverable concerns the demonstrator planned for Deliverable 4.6- Heat Recovery unit.



1 Summary

The conventional mechanical heat recovery system is unattractive for a single-house application or for building retrofit purposes due to its bulky and large size. Existing space heating systems can improve the occupants' comfort and heating fuel efficiency. However, tenants tend to open windows to reach their desired temperature, resulting in greater space heat loss and increased heating fuel usage. Even though the temperature inside the room is optimal, householders still need to ventilate the room for fresh air. Balancing the air exchange of the room can alleviate damage due to moisture as well. Cold ventilation air can cause shrinkage cracks in wood and drywall surfaces slow drying of wetted surfaces, condensation on windows, and growth of mould and mildew.

The proposed innovative WHR: A typical house fitted with the room heat recovery system alone will reduce its annual energy bill by 20%. Small heat recovery and air filtering units can be installed on window frame (see Figure 1). The initial development work of an innovative room heat recovery/ventilation for window frame system has been carried out by the partners. The system uses heat normally lost from the room to bring in and preheat fresh air and save energy.

The key innovations are as follows:

- i. Low cost and high energy efficiency. The room heat recovery unit can recover 70% of the heat needed to make outside air comfortable on its way in the room. The heat recovery uses electronically controlled miniature fans to regulate the airflow in and out reducing energy consumption and ensures optimal ventilation.
- ii. Improve indoor air quality while reducing energy consumption: The window heat recovery unit is ideal for existing buildings and suits new build construction as well. The heat recovery unit can be self-powered using direct current electricity from PV and with minimum wiring. The unit can improve indoor air quality while enhance quality of life,
- iii. Provides optimal ventilation at minimum heat loss,
- iv. Provides smart heat recovery in a more natural way than conventional MHRV, reduce running costs, and high performance.



Fig. 1. 3D view of window integrated system (a), heat recovery unit -integrated to window frame (b), and heat recovery prototype (c)



2 Concept and modelling

Several studies have investigated the impact of ventilation on indoor air temperature. Three categories of key parameters [1] will affect the ventilation efficiency, including external weather conditions, building materials and occupants' behaviours of ventilation control (day/night ventilation), ventilation rate and indoor air temperature settings. As many studies confirmed [2][3][4][5], the occupants' behaviour and indoor air quality are interactively influenced by each other according to the efficiency of ventilation systems.

In recent decades, mechanical ventilation systems have been increasingly used to meet ventilation requirements and dilute indoor-generated pollutants. Numerous studies [6][7][8] have examined the effects of residential mechanical ventilation systems on IAQ, thermal comfort, and/or energy use. Mechanical ventilation systems with heat recovery (MVHR) have become more popular as an energy-efficient solution to provide good IAQ during the heating season [9]. However, mechanical ventilation systems are typically in operation throughout the whole year resulting in high energy consumption for operating the fan [10]. Moreover, due to the lack of financial resources to purchase and install the MVHR system, especially in existing houses, homeowners or landlords are rarely considering this system [11]. Therefore, considering the above-mentioned limitations, it is imperative to develop an energy-efficient, compact, non-instructive and easy-installed heat recovery ventilation system for building retrofit.

Heat recovery technologies can be classified using different criteria [12][13]. For example, Mardiana-Idayu et al. [12] presented a review of heat recovery technologies for building applications, where the different types are divided according to the construction type of the heat exchanger. According to them, they can be classified in fixed-plate [14][15], rotary wheel [16][17], run-around [18][19] and heat pipes [20][21]. Fixed plates are the most used and can achieve high values of efficiency, and the rotary wheel can recover both sensible and latent heat, while the run-around has the advantage of recovering heat from different parts of the building [22]. Heat pipe types have some advantages concerning conventional technologies, such as being suitable for natural ventilation due to their low resistance to airflow, ability to work at the low-temperature difference, and high heat transfer rate in a small cross-section area [22]. Shao et al. [23] presented and conducted the experimental investigation of a low-pressure drop heat recovery device made of heat pipes. They studied the effect of different techniques to increase the heat transfer while not increasing the flow resistance. They found recovery efficiency around 60% and that using wire fins presents the best balance between good thermal performance and low flow resistance.

This work proposed, modelled, and conducted a performance analysis of a window heat recovery system. The developed model is validated against experiments, and a correlation for effective thermal conductivity is proposed. The recovery unit is based on heat pipes and presents high efficiency due to the effective heat transfer in a small cross-section of heat pipes, and it has a lower pressure drop than conventional technologies, which makes this technology suitable for natural ventilation and requirement of less power for fans for application of higher ventilation rate. In addition, the system has no complex structures, which means it is easy to build and install in the building.



2.1 System configurations

Window heat recovery systems are heat exchangers attached to building windows frame to permit heat exchange between exhausted and supplied air during the process of building ventilation, including natural ventilation [2][22][23][1]. An example of integrating the window heat recovery system in the building is presented in Figure 2. Heat pipes have two main parts, the cold side (condenser) and the hot side (evaporator), where heat is transferred from evaporator to condenser [23]. The window heat recovery system works in all four seasons, for example, in winter, its purpose is to recover heat from exhausted air to the supplied fresh air, and in summer, the exhausted air cools the supplied air.

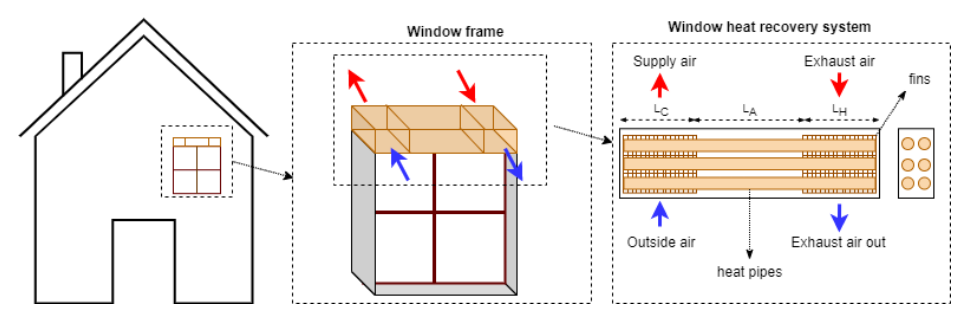


Fig. 2. Window heat recovery system integrated with building (Winter example)

2.2 Numerical modelling

In this study, a window heat recovery system made of two layers ($N_P = 2$), each one containing three heat pipes connected in serial ($N_S = 3$) is considered as reference configuration (**Error! Reference source not found.**). Heat pipes can be defined as passive thermal devices designed to provide effective transport of thermal energy. Nevertheless, modelling the physical phenomena that occur in heat pipes is complex. Nevertheless, the focus of this work is the development of a numerical model able to predict with appropriate accuracy the global performance of window heat recovery systems made of heat pipes. Therefore, for modelling purposes, it is reasonable to consider the heat pipe as a pseudo solid material with a high effective value of thermal conductivity.

Circular fins are used to improve heat transfer on the hot and cold sides of the heat recovery system. **Error! Reference source not found.** presents the total thermal resistance network for a single layer of three heat pipes and the thermal resistances for a single heat pipe.



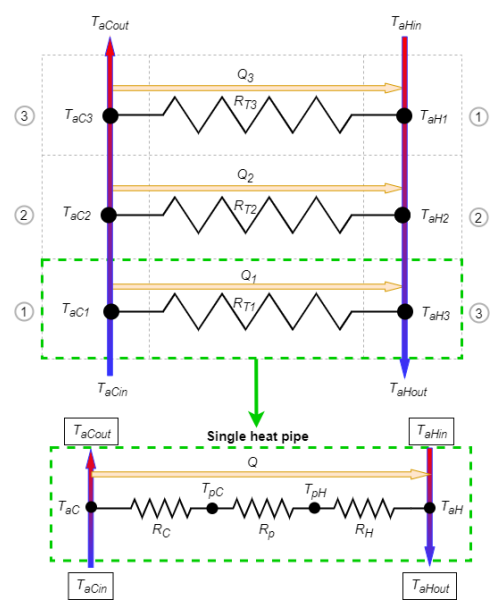


Fig. 3. Thermal resistance network between heat pipes and air in cold and hot sides

In this approach, the window heat recovery system can be modelled as a counter flow heat exchanger. It is assumed that air flowing through the system is divided into equal parts for the number of layers of heat pipes without thermal losses in steady-state conditions. Then, Eqs. (1-2) can be used to describe a single section of heat pipe:

$$Q = \frac{T_{pC} - T_{aC}}{R_C} = \frac{T_{pH} - T_{pC}}{R_p} = \frac{T_{aH} - T_{pH}}{R_H} = \frac{T_{aH} - T_{aC}}{R_T}$$
 Eq. (1)

$$Q = \dot{m}_C C_p (T_{aCout} - T_{aCin}) = \dot{m}_H C_p (T_{aHin} - T_{aHout})$$
 Eq. (2)

where Q is the heat flow through the heat pipe from hot to the cold side, T_{pC} and T_{pH} are the mean temperature of heat pipes in the cold and hot side, T_{aC} and T_{aH} are the mean air temperature on the cold and hot side, R_C and R_H are the thermal resistance (convective), R_p is the conductance thermal resistance of heat pipe, \dot{m}_C and \dot{m}_H are the air mass flow rate, C_p is the specific heat capacity of air, and T_{aCout} , T_{aCin} , T_{aHout} and T_{aHin} are, respectively, inlet and outlet temperature of the air in cold and hot sides. The total thermal resistance R_T , convective and conductance thermal resistances are calculated using:

$$R_T = R_C + R_p + R_H$$
 Eq. (3)

$$R_C = \frac{1}{hA_C}$$
 Eq. (4)

$$R_p = \frac{L_{eff}}{A_p k_{eff}}$$
 Eq. (5)



$$R_H = \frac{1}{hA_H}$$
 Eq. (6)

where h is the convective heat transfer coefficient on the cold and hot side (it is considered the same value for both sides), A_C and A_H are total heat transfer areas, which depend on the number of fins N_f in each side, the distance between fins d_{btf} , diameter D_f and thickness f_{th} (it is considered both sides with the same number of fins). The parameters L_{eff} and k_{eff} are the effective length and thermal conductivity of heat pipe, respectively, and A_p is the cross-section area of the heat pipe ($A_p = \pi(D_p/2)^2$). The effective length is calculated using [24]:

$$L_{eff} = L_A + \frac{L_C + L_H}{2}$$
 Eq. (7)

in which L_A is the adiabatic length and L_C and L_H are the length of the cold and hot sides, respectively (see **Error! Reference source not found.**). The effective thermal conductivity is estimated according to the experimental work described in Section 3.1.1.

2.2.1 Convective heat transfer coefficient

For convective heat transfer coefficient in cold and hot sides, the following correlation for the average Nusselt number \overline{Nu} from the work of Romero-Méndez et al. [25] is used with some modifications:

$$\overline{Nu} = \frac{hD_p}{k_a} = F \text{RePr} \frac{WS}{A_f/D_p^2 + \pi S} \left[1 - \exp\left(-\frac{1.32 \text{Pr}^{4/3} W^{1/2}}{Re^{1/2} S}\right) \right] \quad \text{Eq. (8)}$$

where k_a is the thermal conductivity of air, F is a calibration factor, R is the Reynolds number, R is the Prandtl number, R is the nondimensional diameter of the fins, R is the nondimensional distance between fins, R is the total surface area of a single fin (the circular and annular surfaces area), where R is the nondimensional fin surface area. The Reynold number is calculated using:

$$Re = \frac{\rho V D_p}{\mu}$$
 Eq. (9)

in which ρ , μ and V are the air density, dynamic viscosity, and velocity, respectively. The velocity of air is obtained from mass flow rate (\dot{m}_C and \dot{m}_H), density, and the total cross-section area of void space between fins.

The correlation from Eq. (8) is originally obtained by analysing a rectangular fin, but it was adapted for a case of a circular fin in this work. According to Stark et al. [26], this correlation predicted the convective heat transfer coefficient. Furthermore, the correlation was obtained considering a single pair of fins, significantly decreasing its accuracy in predicting the Nusselt number when a high number of fins is used. For this reason, a calibration factor F is included in the correlation and adjusted to agree with data from the experiments presented in Section 3.1.1.



2.2.2 Solution method, performance and parameters

The equations were solved using GNU Octave software through an iterative process. The procedure is presented in the flow chart of **Error! Reference source not found.**.

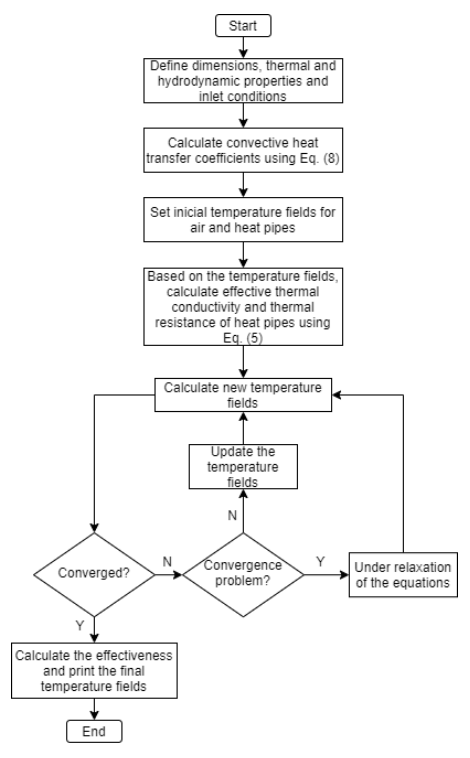


Fig. 4. The flowchart of the solution method

When the governing equations are solved, the effectiveness of the window heat recovery is calculated using the following equation:

$$\varepsilon = \frac{\dot{m}_{C}C_{p}(T_{aCout} - T_{aCin})}{\min(\dot{m}_{C}C_{p}; \, \dot{m}_{H}C_{p})(T_{aHin} - T_{aCin})}$$

$$= \frac{\dot{m}_{H}C_{p}(T_{aHin} - T_{aHout})}{\min(\dot{m}_{C}C_{p}; \, \dot{m}_{H}C_{p})(T_{aHin} - T_{aCin})}$$
Eq. (10)

where $\min(\dot{m}_C C_p; \dot{m}_H C_p)$ is the minimum value between the product's mass flow rate and specific heat capacity of the cold and hot sides. The geometric parameters of the reference configuration of the window heat recovery used in the simulations are presented in Table 1. The thermal and hydrodynamic properties of air are considered constant for a temperature of 25 °C. Table 1 Geometric parameters of the window heat recovery system

Parameter	Value
$L_C = L_H \text{ (cm)}$	50
L_A (cm)	10
N_f	134



D_p (cm)	2
D_f (cm)	4
f_{th} (mm)	1.5
d_{btf} (mm)	2.25
N_P	2
N_S	3

2.2.3 CFD modelling method

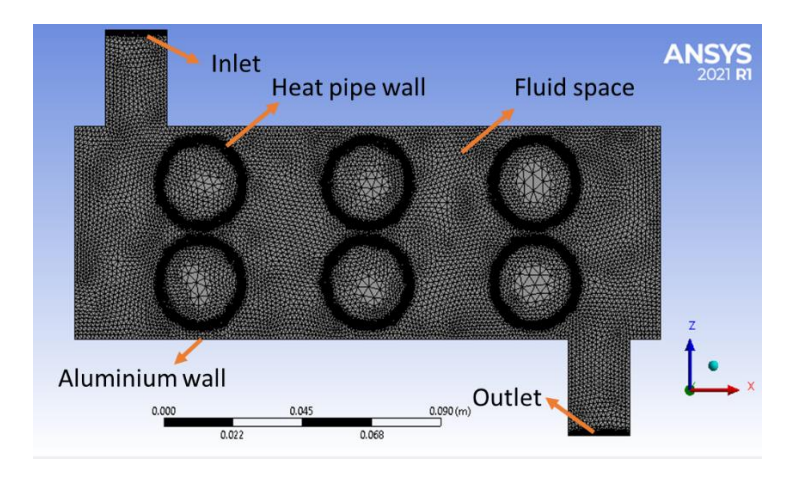
The CFD code ANSYS 2021 R1 was used in this study to validate the accuracy of heat pipe effectiveness along with simulating the air and velocity distribution in the small room connected to the heat pipe model. The simulation of the heat pipe and the attached room was considered the steady state with a two-dimensional computational model where the CFD code used the Finite Volume Method (FVM) with the Semi Implicit Method for Pressure Linked Equations (SIMPLE) velocity-pressure coupling algorithm. The turbulent element of the airflow was modelled using the Realisable $k-\varepsilon$ turbulence model with enhanced wall functions to get further improved prediction for flows involving rotation and boundary layers under strong adverse pressure gradients inside the heat pipe model [27][28][29]. Second-order upwind schemes were adopted for the calculation. Before the simulation process, the under-relaxation factors for pressure, momentum, k and ε were set to 0.2, 0.25, 0.25 and 0.25 for both heat pipe and room models, respectively. Convergence steps were set to 10000, where the convergence was monitored, and iterations were ended when all residuals showed no further declinations with the increasing iterations. The governing equations were fully introduced in the ANSYS FLUENT Guide [29].

The geometry of heat pipe and room models was created using the SpaceClaim (FLUENT preprocessor) in the ANSYS 2021 Workbench. According to the configuration of the heat pipe and room models described in Sections 2.2, the established geometry was imported into ANSYS mesh processor where the fluid surfaces areas were not extracted from the model since both the conduction and convection models were investigated in this study. The constructed mesh was used to discretise the surface of the computational domains. All triangles method was used for heat pipe model to acquire the best split near heat pipe sections whereas Quadrilateral method for the small room model. The size of mesh elements was improved smoothly to solve those sections with high gradient mesh to require more accurate results of the velocity and temperature fields near the velocity inlet, pressure outlet, and heat pipe walls [30][31]. Furthermore, level 3 refinements were applied in these areas as well. The mesh element size of the heat pipe and room models for surfaces and edges were 10 mm and 5 mm, with the total element number of 348340 and 330870, respectively. The modelled meshes of the heat pipe and small room models using ANSYS Mesh are shown in (b)

(a) and (b)



(b).



(a)

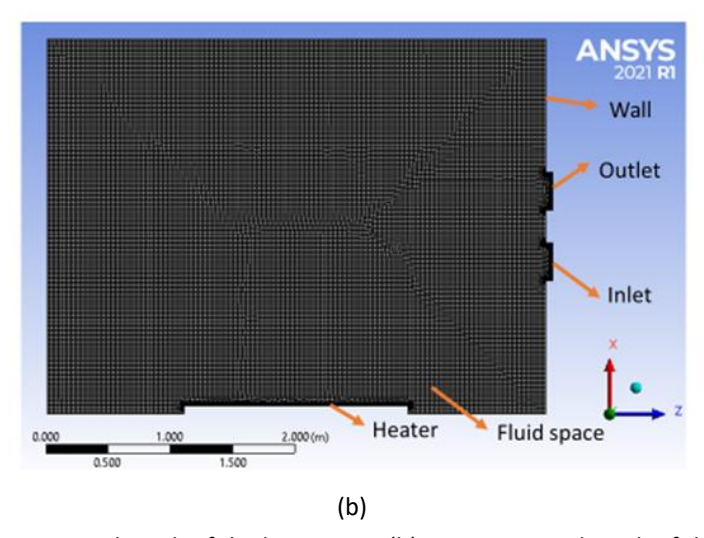


Fig. 5. (a) Computational mesh of the heat pipes. (b) Computational mesh of the small room



3 Experimental and validation

3.1 Experimental

The window heat recovery prototype presented in Fig. 6 was tested under different conditions. The temperature was recorded in different locations, as identified in **Error! Reference source not found.** (T_1 to T_9 are temperature sensors), and then the average temperature on the two sides of the pipes and the average heat flux are calculated.

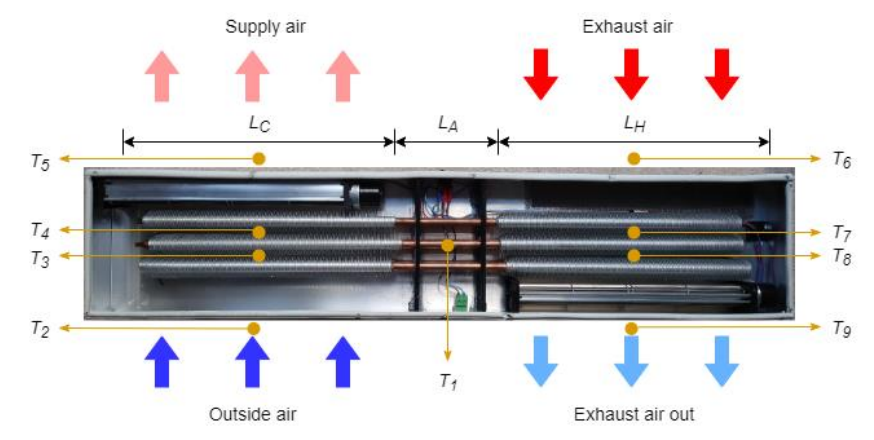


Fig. 6. Window heat recovery prototype used in the experiments

3.1.1 Determination of effective thermal conductivity

For the determination of effective thermal conductivity, the following relation resulted from the combination of Eqs. (1) and (5) is used:

$$k_{eff} = \frac{Q_{av}L_{eff}}{A_p(T_{pH} - T_{pC})}$$
 Eq. (11)

where Q_{av} is the mean heat flowing through a single heat pipe and T_{pH} and T_{pC} are, respectively, the average heat pipe hot side temperature and cold side temperature. The experiments are conducted for $\dot{m}_C = \dot{m}_H$ This means that the temperature profiles from inlet to outlet on each side can be considered approximately linear. To simplify the approach to estimating the effective thermal conductivity without compromising the accuracy, it is assumed that the total heat flux is divided into equal parts for all heat pipes $Q_{av} = Q_T/(N_P N_S)$. The total heat flux Q_T is calculated using Eq. (2), the temperature recorded in locations T_2 , T_5 , T_6 and T_9 and the mass flow rate. The length L_{eff} is calculated from Eq. (7), and the temperature difference $T_{pH} - T_{pC}$ is calculated using the average temperature difference between T_2 to T_5 and T_9 to T_6 . The inlet temperature of the cold and hot sides are changed according to

Table 2, and the mass flow rate is fixed in $\dot{m}_C = \dot{m}_H = 69.1$ m³/h. Fig. 7 presents the obtained effective thermal conductivity for the temperature differences between the hot and cold sides.



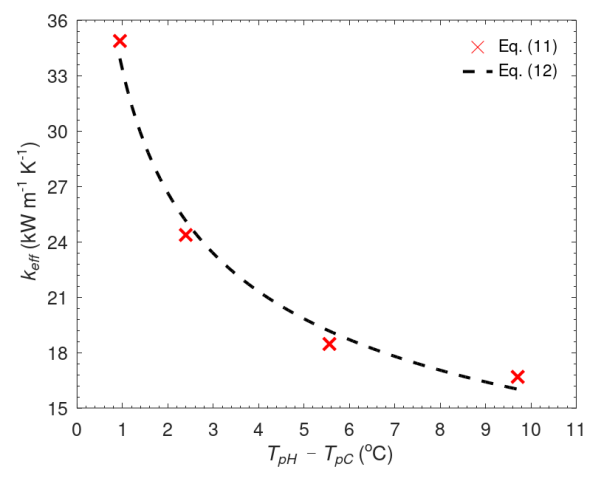


Fig. 7. Effective thermal conductivity for the temperature differences

To obtain a correlation to be used in the numerical model, the data from **Error! Reference source not found.** is fitted using a power-law curve, where the following equation with $R^2 = 0.985$ is obtained:

$$k_{eff} = 33298.8(T_{pH} - T_{pC})^{-0.322}$$
 Eq. (12)

3.2 Validation

3.2.1. Analytical formulation

After determining effective thermal conductivity, the calibration factor F, introduced in Eq. (8), was adjusted to minimise the difference between numerical and experiments, where a value of F=25 was found. This value and the proposed effective thermal conductivity correlation were then used in the simulations. The temperature distribution before and after each heat pipe measured during the experiments and obtained from the numerical model for four different test conditions are presented in Fig. 8.



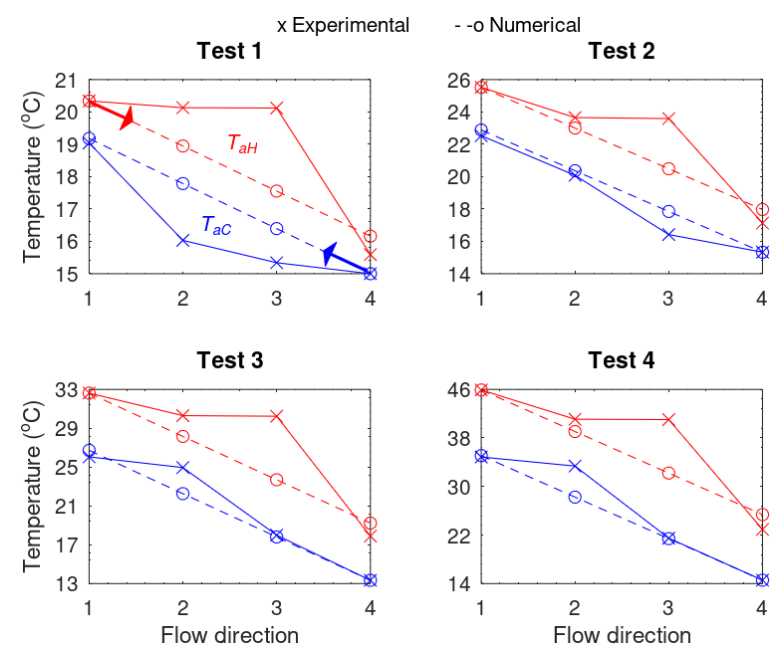


Fig. 8. Comparison between experimental and numerical results for different test conditions

There are some minor differences between measurements and numerical results, but it can be considered that the numerical model can predict reasonably the outlet temperature of air (the most important) on each side. The comparison between outlet temperature for the four test conditions obtained from experimental (Exp.) and numerical (Num.) are presented in Table 2.

Table 2: Comparison between measured and modelled outlet temperature

	Test 1		Test 2		Test 3		Test 4	
	Exp.	Num.	Exp.	Num.	Exp.	Num.	Exp.	Num.
T_{aCin} (°C)	<u>.</u>	15	1	5.3	1	3.4	1	4.6
T_{aCout} (°C)	19.0	19.2	22.5	22.9	26.0	26.7	34.9	35.1
T_{aHin} (°C)	20.4		25.5		32.6		45.9	
T_{aHout} (°C)	15.6	16.2	17.1	18.0	17.9	19.2	22.9	25.4

According to the results presented in

Table 2, the maximum difference between measured and modelled outlet temperature is always on the hot side, which are 3.8%, 5.3%, 7.3% and 10.9%, respectively, for tests 1, 2, 3 and 4. This difference increase when we increase the temperature range, which can be explained due to thermal losses not accounted for in the numerical model. According to this result, it is considered that the model can be used to study the performance of the window heat recovery system for other conditions.



3.2.2. CFD validation

Apart from the analytical formulation, the CFD simulation of the hot and cold side temperature was conducted to compare with the numerical results. Fig. 9(a) and Fig. 9(b) show the temperature and velocity distribution profile of the model with the cold inlet temperature of 15 °C and inlet velocity of 0.93 m/s. The comparison between hot and cold outlet temperature for the four tests conditions obtained in CFD simulation (CFD) and numerical (Num.) are presented in 3. Minor differences between the two methods exist, however, the discrepancies of hot side outlet temperature for CFD simulation and numerical method gradually increase with the more considerable temperature differences, which are 2.4%, 2.6%, 2.8% and 3.2% for tests 1, 2, 3 and 4. The reason may be ascribed to that 1) The iteration has not fully converged; 2) The representation of the governing flow equations and other physical models as algebraic expressions in a discrete domain of space and time; 3) The meshing grid has not been precisely refined; 4) Little computing values per cell and resulting interpolation errors.

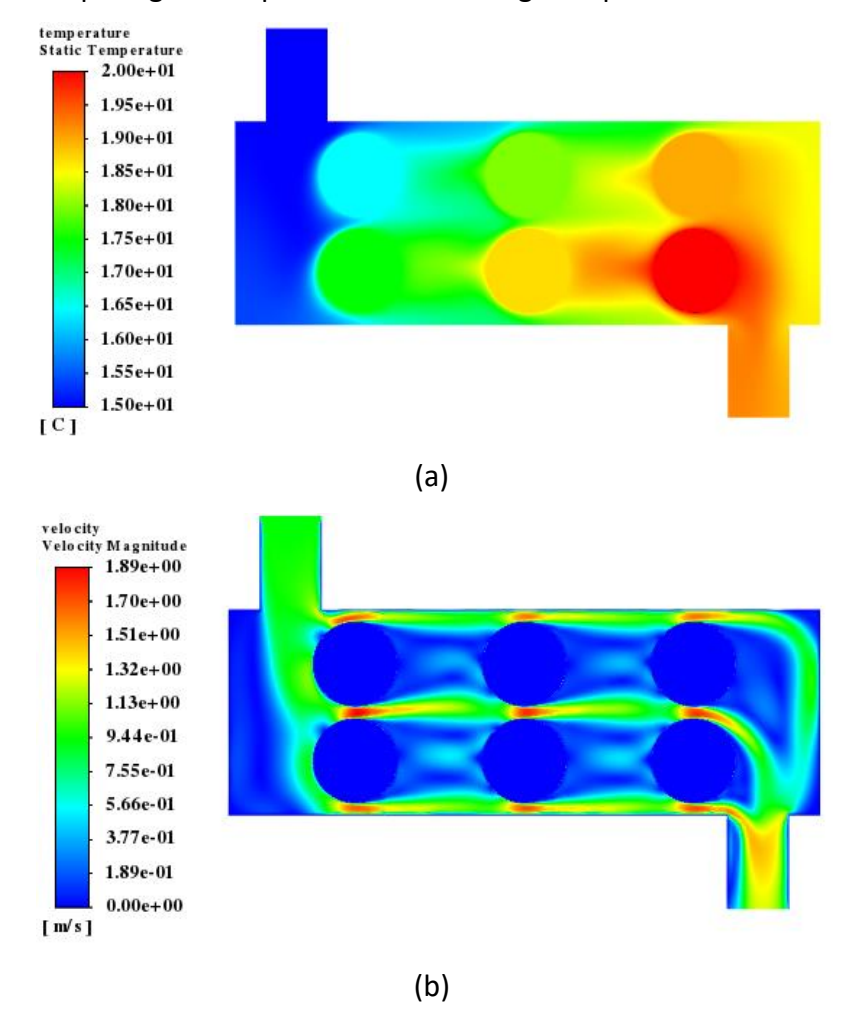


Fig. 9. CFD simulation results with an inlet temperature of 15 °C and inlet velocity of 0.93 m/s: (a) Temperature and (b) velocity magnitude

Table 3 Comparison between CFD simulation and numerical outlet temperatures





	Test 1		Test 2		Test 3		Test 4	
	CFD	Num.	CFD.	Num.	CFD.	Num.	CFD.	Num.
T_{aCin} (°C)	<u>-</u>	15	1	5.3	1	3.4	1	4.6
T_{aCout} (°C)	19.1	19.2	22.5	22.9	26.1	26.7	35.2	35.1
T_{aHin} (°C)	20.4		25.5		32.6		45.9	
T_{aHout} (°C)	15.8	16.2	17.5	18.0	18.7	19.2	24.6	25.4



4 Results and discussion

4.1 Parametric analysis

After model development and validation, it can be used to study the performance of the window heat recovery system for different conditions. In this section, three parameters upon the WHR thermal effectiveness are analysed with the most significant parameter of ventilation rate. Besides, temperature differences between the cold inlet and the hot outlet also have a noticeable impact on the thermal effectiveness. Furthermore, heat pipe layers have a relatively low influence.

The mass flow rate in the hot and cold side is always considered the same ($\dot{m}_C = \dot{m}_H$) and the geometric reference parameters presented in **Error! Reference source not found.** are used. Fig. 10 presents the temperature profile in the air and heat pipe along the flow direction. The profile is linear because of the approaches and the same mass flow rate used on each side.

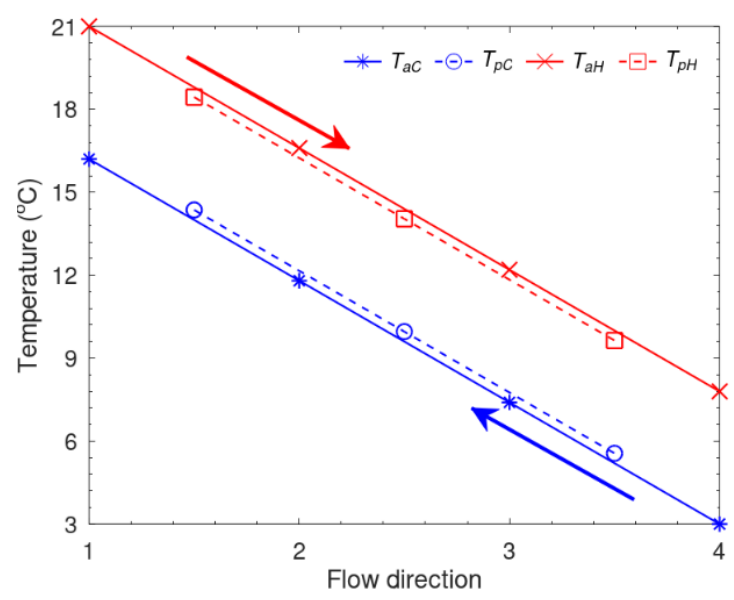


Fig. 10. Temperature profile in air and heat pipe along the flow direction of the window heat recovery system

The inlet temperature, mass flow rate, outlet temperature and effectiveness for the results are presented in Fig. 10, with $T_{aCin}=3$ °C, $T_{aHin}=21$ °C, $\dot{m}_{C}=\dot{m}_{H}=60$ m³/h, $T_{aCout}=16.2$ °C, $T_{aHout}=7.8$ °C, respectively which resulted in the effectiveness of $\varepsilon=73.3\%$.

Numerical simulation results indicate that the thermal effectiveness slightly drops with the rise of the maximum temperature differences between the cold outside air and hot exhaust air, as shown in Fig. 11. Temperature differences from 10 °C, 20 °C to 30 °C are investigated with the ventilation rates raised between 10 and 60 m³/h. It is figured out that the thermal effectiveness is similar in the range of 94.5% and 95.7% when a low ventilation rate of 10 m³/h. However, the thermal effectiveness decreases between 69.5% and 77.3% when the ventilation rate rises to 60 m³/h. Thus, the thermal effectiveness declining rates are calculated as 0.06%/°C, 0.14%/°C, 0.22%/°C, 0.285%/°C, 0.345%/°C and 0.39%/°C with varied ventilation rates of 10 m³/h, 20 m³/h, 30 m³/h, 40 m³/h, 50 m³/h and 60 m³/h, respectively. Meanwhile, it is also figured out that the ventilation rates have the most significant impact on the improvement of thermal effectiveness,



which reveals that the heat transfer coefficient has noticeable degradation with the rise of the ventilation rate from $10 \text{ m}^3\text{/h}$ to $60 \text{ m}^3\text{/h}$. The thermal effectiveness is dropped by 18.4%, 22.4% and 25.0% with the rise of ventilation rate of $50 \text{ m}^3\text{/h}$ when the temperature differences are 10 °C, 20 °C and 30 °C, respectively.

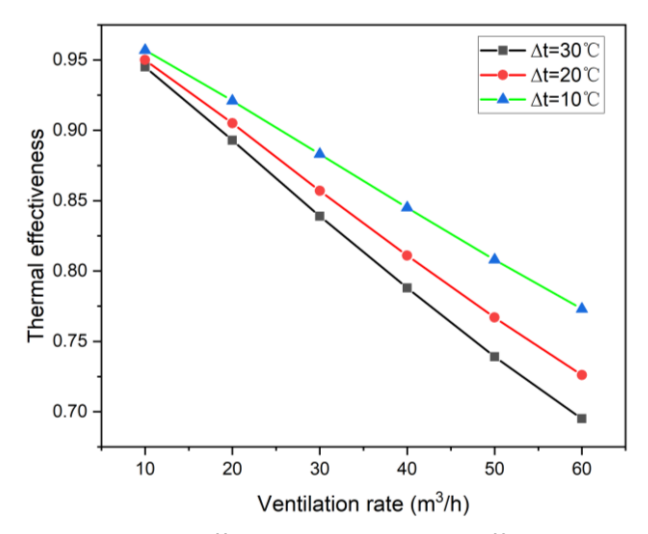


Fig. 11. Impact of maximum temperature difference on the thermal effectiveness with ventilation rate varied between 10 to $60 \text{ m}^3/\text{h}$

It is figured out that the increase of heat pipe numbers has a significant impact on the improvement of thermal effectiveness, as shown in Fig. 12, which reveals that the heat transfer coefficient has a noticeable upgrade when the heat pipe layers increase from $N_p=2$ to $N_p=3$, with total heat numbers increasing from 6 to 9. Results indicate that the thermal effectiveness is upgraded from 94.5% to 97.0% when a low ventilation rate of 10 m³/h. However, the thermal effectiveness decreased between 69.5% and 83.9% when the ventilation rate rises to 60 m³/h. Thus, the thermal effectiveness decreasing rates are calculated as 1.25%/layer, 2.6%/layer, 4.05%/layer, 5.25%/layer, 6.35%/layer and 7.2%/layer with varied ventilation rates of 10 m³/h, 20 m³/h, 30 m³/h, 40 m³/h, 50 m³/h and 60 m³/h, respectively.



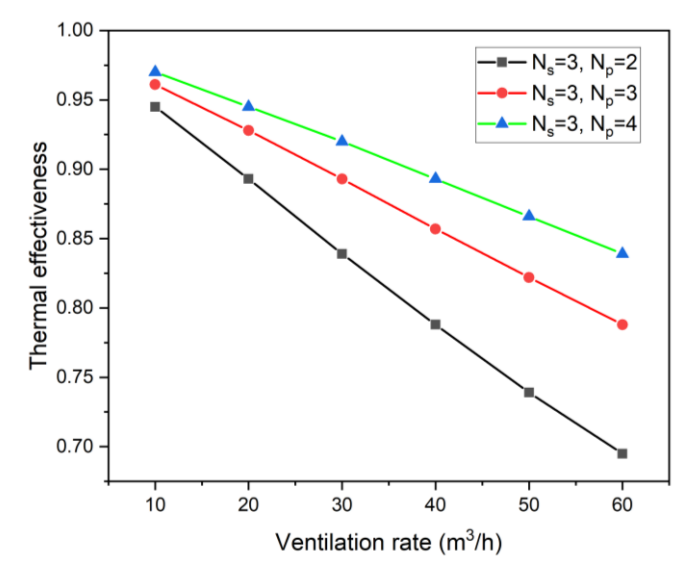


Fig. 12. Impact of heat pipe numbers on the thermal effectiveness with ventilation rate varied between 10 to 60 $\,\mathrm{m}^3/\mathrm{h}$

According to the CFD simulation results, the relative total pressure contour of the WHR system with the cold inlet temperature of 15 °C and ventilation rate of 10 m³/h is shown in Fig. 13. The total pressure drop between the inlet and outlet sides is 4.12 Pa, with the former pressure of 4.69 Pa and the latter one of 0.57 Pa. Meanwhile, the pressure drop increases with the rise of ventilation rates from 10 - 60 m³/h, where the pressure drop is from 4.12 Pa to 77.9 Pa correspondingly, as shown in **Error! Reference source not found.**. To obtain a correlation that can be used in the calculation of pressure drop under various ventilation rates, the data from Fig. 14 are fitted using an exponential expression, where the following equation Eq. (13) with $R^2 = 0.999$ is obtained:

$$\Delta P = 0.0931 V_r^{1.6417}$$
 Eq. (13)

where ΔP is the total pressure drop between inlet and outlet sides (Pa) and V_r is the ventilation rate (m³/h).

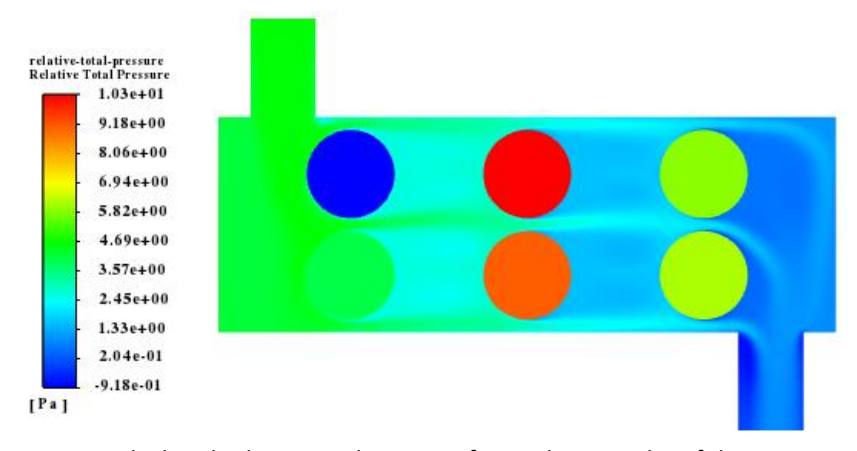


Fig. 13. CFD calculated relative total pressure from inlet to outlet of the WHR system



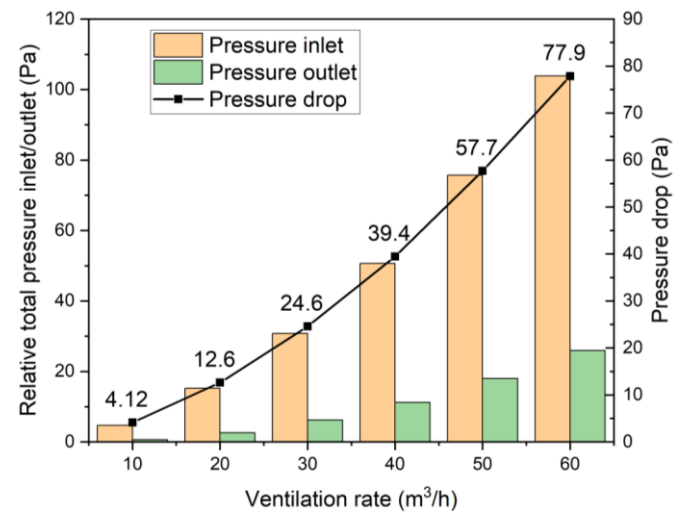


Fig. 14. System pressure drop under ventilation rates varied between 10 – 60 m³/h

4.2 Thermal comfort

The vertical and horizontal air temperature and velocity differences are investigated to analyse the air thermal comfort parameters distribution. It was determined by recording the temperature and velocity values at eight layers, representing distances from the WHR inlet between 0.5 m and 4.0 m. In addition, five horizontal distances are also recorded in each layer. Firstly, the indoor thermal comfort improvement is analysed by comparing the existence of the WHR system under the ventilation rate of 10 m³/h, as shown in Fig. 15 (without) and Fig. 16(a) (with) the heat recovery. It is discovered that the maximum indoor air temperature difference drops from 4.5 °C to 3 °C, where the average temperature has a significant increase from 13.5 °C to 22.5 °C. However, the maximum indoor air velocity rises from 0.47 m/s to 0.9 m/s due to the large pressure difference near the inlet region caused by the inlet-outlet backflow of the WHR system at 0.5 m vertical layer and 1.5 m horizontal distance. Additionally, the air velocity disturbance is weakened in the region away from the inlet.

Fig. 16 reveals the impact of the WHR ventilation rates on the indoor thermal comfort in terms of the air temperature and velocity distribution, under (a) 10 m³/h, (b) 30 m³/h and (c) 60 m³/h air change rates. With the increment of the ventilation rate, the indoor air temperature rises to 22.5 °C, 23 °C and 23.3 °C, respectively. The air temperature disturbance is weakened with maximum indoor temperature differences reaching 2.8 °C, 2.5 °C and 2.2 °C, respectively. On the contrary, the average indoor air velocity increases from 0.2 m/s to 0.7 m/s and 1.1 m/s, respectively, due to the rise of the ventilation rate. Besides, the air velocity disturbance is strengthened along with the increment of indoor air velocity.



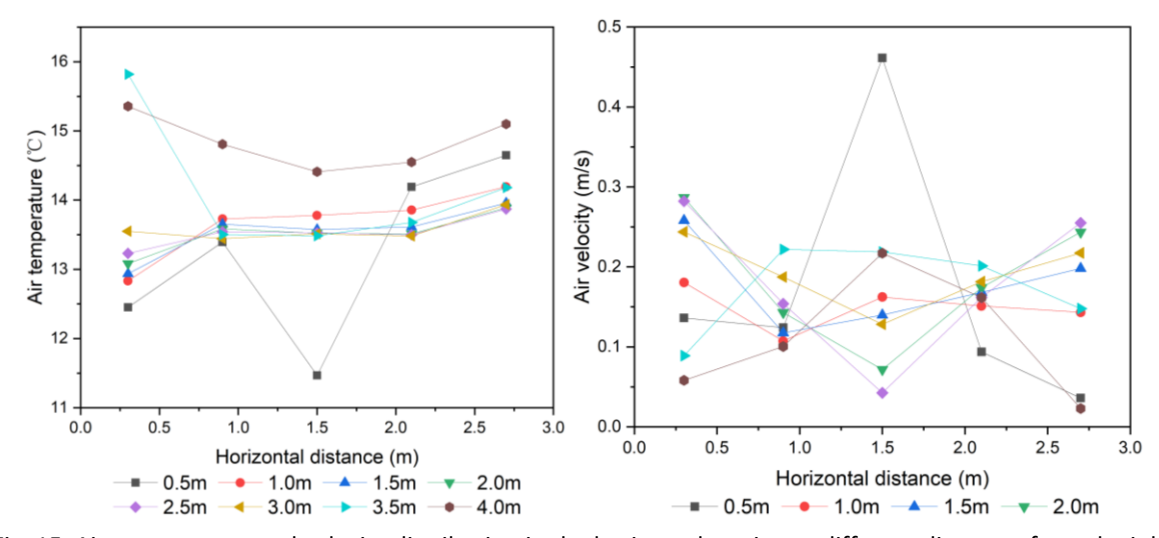
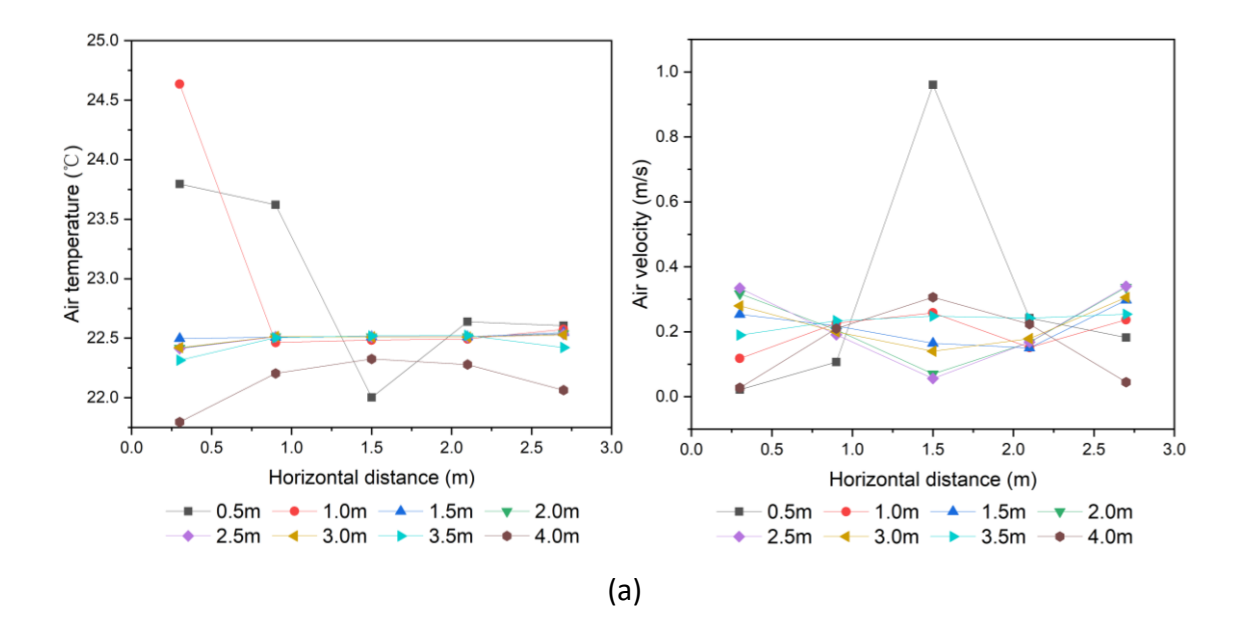


Fig. 15. Air temperature and velocity distribution in the horizontal section at different distances from the inlet under 10 $\rm m^3/h$ ventilation rate without heat recovery





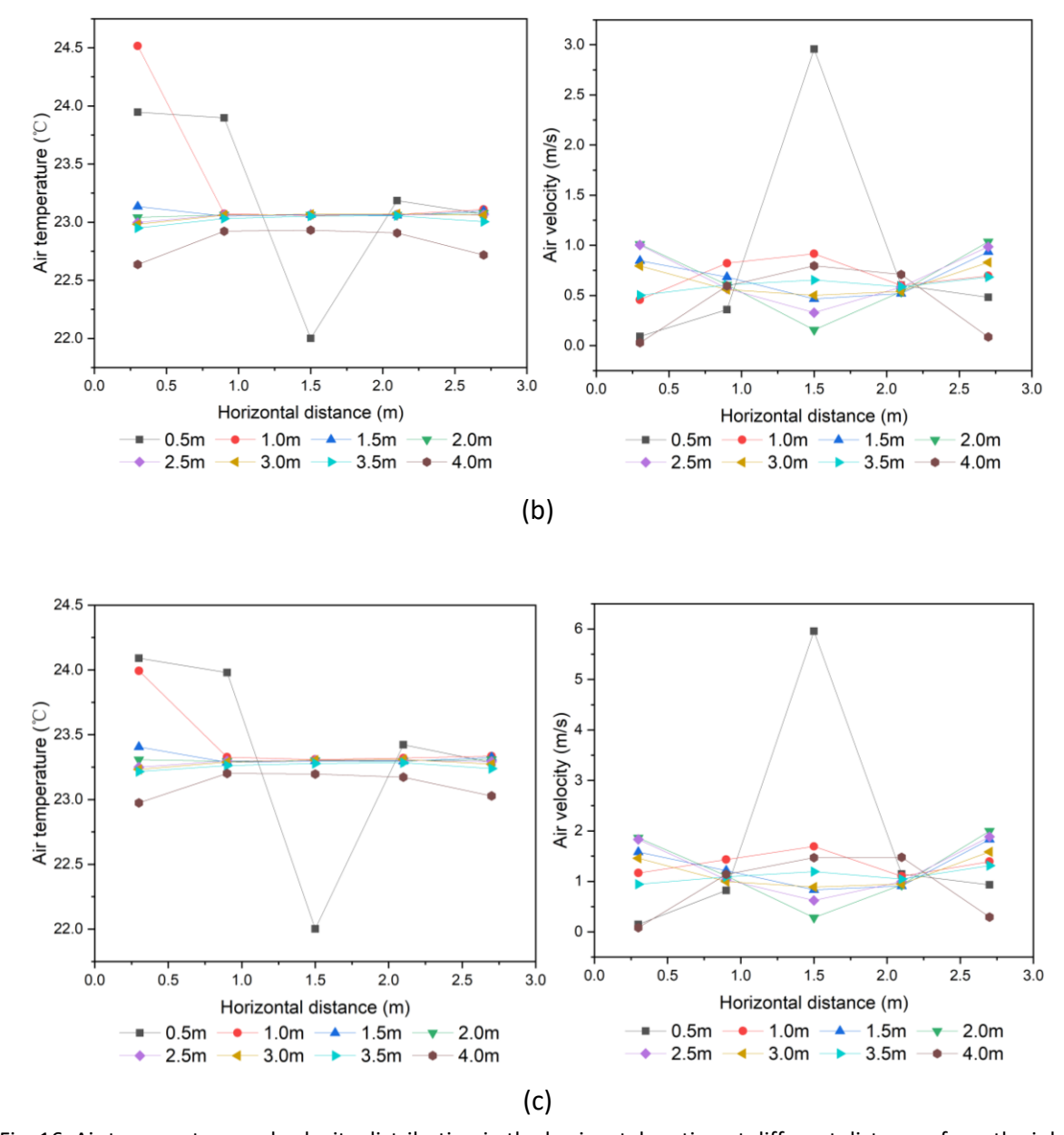


Fig. 16. Air temperature and velocity distribution in the horizontal section at different distances from the inlet under 10 $\rm m^3/h$ (a), 30 $\rm m^3/h$ (b) and 60 $\rm m^3/h$ (c) ventilation rates with heat recovery



5 Conclusions

This work presents the numerical and experimental performance of the window heat recovery (WHR) system made of heat pipes. The numerical model is validated with the experiments and used to study the system for different working conditions and analyse its effect on energy performance in building and thermal comfort. The following conclusions can be drawn:

- The effectiveness of window heat recovery made of heat pipes depends on ventilation rate and temperature difference between exhausted and supplied air.
- Higher ventilation rate and temperature difference decrease the effectiveness. For ventilation rate between 10 60 m³/h and temperature difference 10 30 °C, effectiveness between 65 95% and pressure drop 4 80 Pa are obtained. For performance in building, the power consumption can be reduced between 3 24% and the thermal comfort increased.
- Ventilation rates have the most significant impact on thermal effectiveness improvement, where the thermal effectiveness is similar in the range of 94.5% 95.7% at a lower ventilation rate (10 m³/h), whereas it declines to 69.5% and 77.3% at a higher ventilation rate (60 m³/h). The thermal effectiveness is dropped by 18.4%, 22.4% and 25.0% with the rise of ventilation rate of 50 m³/h when the temperature differences are 10 °C, 20 °C and 3 °C, respectively.
- Based on CFD simulation results, the pressure drop increases with the rise of ventilation rates from 10 – 60 m³/h, where the pressure drop is from 4.12 Pa to 77.9 Pa correspondingly.
- The maximum indoor air temperature difference drops from 4.5 °C to 3 °C, where the average temperature has a significant increase from 13.5 °C to 22.5 °C with different distances from the WHR inlet between 0.5 m and 4.0 m. Nonetheless, the maximum indoor air velocity shows the contrary trend due to the inlet-outlet backflow of the WHR system at 0.5 m vertical layer and 1.5 m horizontal distance. Additionally, the air velocity disturbance is affected by the distance from the inlet.



References

- [1] S. Zhang, Z. Ai, Z. Lin, Novel demand-controlled optimisation of constant-air-volume mechanical ventilation for indoor air quality, durability and energy saving, Appl. Energy. 293 (2021) 116954. https://doi.org/10.1016/j.apenergy.2021.116954.
- [2] O. Guerra Santin, L. Itard, H. Visscher, The effect of occupancy and building characteristics on energy use for space and water heating in Dutch residential stock, Energy Build. 41 (2009) 1223–1232. https://doi.org/10.1016/j.enbuild.2009.07.002.
- [3] W. Biesiot, K.J. Noorman, Energy requirements of household consumption: A case study of The Netherlands, Ecol. Econ. 28 (1999) 367–383. https://doi.org/10.1016/S0921-8009(98)00113-X.
- [4] V. Fabi, R.V. Andersen, S. Corgnati, B.W. Olesen, Occupants' window opening behaviour: A literature review of factors influencing occupant behaviour and models, Build. Environ. 58 (2012) 188–198. https://doi.org/10.1016/j.buildenv.2012.07.009.
- [5] H. Cho, D. Cabrera, S. Sardy, R. Kilchherr, S. Yilmaz, M.K. Patel, Evaluation of performance of energy efficient hybrid ventilation system and analysis of occupants' behavior to control windows, Build. Environ. 188 (2021). https://doi.org/10.1016/j.buildenv.2020.107434.
- [6] A. Paone, J.P. Bacher, The impact of building occupant behavior on energy efficiency and methods to influence it: A review of the state of the art, Energies. 11 (2018). https://doi.org/10.3390/en11040953.
- [7] I. Kang, A. McCreery, P. Azimi, A. Gramigna, G. Baca, K. Abromitis, M. Wang, Y. Zeng, R. Scheu, T. Crowder, A. Evens, B. Stephens, Indoor air quality impacts of residential mechanical ventilation system retrofits in existing homes in Chicago, IL, Sci. Total Environ. 804 (2021) 150129. https://doi.org/10.1016/j.scitotenv.2021.150129.
- [8] Z. Tian, L. Yang, X. Wu, Z. Guan, A field study of occupant thermal comfort with radiant ceiling cooling and overhead air distribution system, Energy Build. 223 (2020) 109949. https://doi.org/10.1016/j.enbuild.2020.109949.
- [9] B. Yassine, K. Ghali, N. Ghaddar, I. Srour, G. Chehab, A numerical modeling approach to evaluate energy-efficient mechanical ventilation strategies, Energy Build. 55 (2012) 618–630. https://doi.org/10.1016/j.enbuild.2012.08.042.
- [10] P. Clarke, Module 141: MVHR for energy-efficient ventilation and summer cooling, CIBSE J. (2019).
- [11] F. Babota, Mechanical Ventilation Systems With Heat Recovery for Refurbishment Projects and New Buildings, Bull. Polytech. Inst. Jassy. (2014).
- [12] J. Krieger, D.L. Higgins, Housing and health: Time again for public health action, Am. J. Public Health. 92 (2002) 758–768. https://doi.org/10.2105/AJPH.92.5.758.



- [13] A. Mardiana-Idayu, S.B. Riffat, Review on heat recovery technologies for building applications, Renew. Sustain. Energy Rev. 16 (2012) 1241–1255. https://doi.org/10.1016/j.rser.2011.09.026.
- [14] P.M. Cuce, S. Riffat, A comprehensive review of heat recovery systems for building applications, Renew. Sustain. Energy Rev. 47 (2015) 665–682. https://doi.org/10.1016/j.rser.2015.03.087.
- [15] S. Shen, W. Cai, X. Wang, Q. Wu, H. Yon, Investigation of liquid desiccant regenerator with fixed-plate heat recovery system, Energy. 137 (2017) 172–182. https://doi.org/10.1016/j.energy.2017.07.024.
- [16] M. Nasif, R. Al-Waked, G. Morrison, M. Behnia, Membrane heat exchanger in HVAC energy recovery systems, systems energy analysis, Energy Build. 42 (2010) 1833–1840. https://doi.org/10.1016/j.enbuild.2010.05.020.
- [17] J.K. Calautit, D. O'Connor, P.W. Tien, S. Wei, C.A.J. Pantua, B. Hughes, Development of a natural ventilation windcatcher with passive heat recovery wheel for mild-cold climates: CFD and experimental analysis, Renew. Energy. 160 (2020) 465–482. https://doi.org/10.1016/j.renene.2020.05.177.
- [18] C.E.L. Nóbrega, N.C.L. Brum, Modeling and simulation of heat and enthalpy recovery wheels, Energy. 34 (2009) 2063–2068. https://doi.org/10.1016/j.energy.2008.08.016.
- [19] A. Vali, C.J. Simonson, R.W. Besant, G. Mahmood, Numerical model and effectiveness correlations for a run-around heat recovery system with combined counter and cross flow exchangers, Int. J. Heat Mass Transf. 52 (2009) 5827–5840. https://doi.org/10.1016/j.ijheatmasstransfer.2009.07.020.
- [20] J.C.Y. WANG, Practical thermal design of run-around air-to-air heat recovery system, Heat Recover. Syst. 5 (1985) 493–501.
- [21] Y.H. Yau, M. Ahmadzadehtalatapeh, A review on the application of horizontal heat pipe heat exchangers in air conditioning systems in the tropics, Appl. Therm. Eng. 30 (2010) 77–84. https://doi.org/10.1016/j.applthermaleng.2009.07.011.
- [22] E. Gedik, M. Yilmaz, H. Kurt, Experimental investigation on the thermal performance of heat recovery system with gravity assisted heat pipe charged with R134a and R410A, Appl. Therm. Eng. 99 (2016) 334–342. https://doi.org/10.1016/j.applthermaleng.2015.12.075.
- [23] L. Shao, S.B. Riffat, G. Gan, Performance of heat recovery in passive stack ventilation systems, in: CIBSE Natl. Conf., 1998: pp. 174–181.
- [24] M. Zhu, J. Huang, M. Song, Y. Hu, Thermal performance of a thin flat heat pipe with grooved porous structure, Appl. Therm. Eng. 173 (2020) 115215. https://doi.org/10.1016/j.applthermaleng.2020.115215.
- [25] R. Romero-Méndez, M. Sen, K.T. Yang, R. McClain, Effect of fin spacing on convection in a plate fin and tube heat exchanger, Int. J. Heat Mass Transf. 43 (2000) 39–51. https://doi.org/10.1016/S0017-9310(99)00120-9.



- [26] J.R. Stark, T.L. Bergman, Prediction of convection from a finned cylinder in cross flow using direct simulation, turbulence modeling, and correlation-based methods, Numer. Heat Transf. Part A Appl. 71 (2017) 591–608. https://doi.org/10.1080/10407782.2016.1277929.
- [27] H. Seyyedvalilu, Difference between standard and realisable k-epsilon model, (n.d.). https://www.researchgate.net/post/Difference-between-standard-and-realizable-k-epsilon-model (accessed September 28, 2021).
- [28] B. Andersson, R. Andersson, L. Håkansson, M. Mortensen, R. Sudiyo, B. Van Wachem, Computational Fluid Dynamics for Engineers, Cambridge University Press, Cambridge, 2011. https://doi.org/10.1017/CBO9781139093590.
- [29] J.K. Calautit, B.R. Hughes, Measurement and prediction of the indoor airflow in a room ventilated with a commercial wind tower, Energy Build. 84 (2014) 367–377. https://doi.org/10.1016/j.enbuild.2014.08.015.
- [30] ANSYS Fluent User's Guide, ANSYS, Inc., Southpointe, 2013.
- [31] J.K. Calautit, B.R. Hughes, Wind tunnel and CFD study of the natural ventilation performance of a commercial multi-directional wind tower, Build. Environ. 80 (2014) 71–83. https://doi.org/10.1016/j.buildenv.2014.05.022.